HiSST: International Conference on
High-Speed Vehicle Science Technology
26–29 November 2018, Moscow, Russia

Numerical study on wide range operation of a generic Freejet Engine

Di Lu [1], Fang Chen [2] Igor N. Borovik[3] Hong Liu[4]

Abstract

The dual-mode scramjet seems to be a promising propulsion system of high-speed aircraft that is designed to perform well in a wide range of flight conditions. Two typical mechanisms have already been proposed to achieve mode transition including variable geometry without thermal choke and fixed geometry with thermal choke. However, the former brings about the problem of complex structure and overweight, while the latter faces the challenge of heat regulation and narrow operation range. In this paper, a generic freejet engine has been explored to find a better way to operate in a wider range. Numerical studies with CFD ++ 2D RANS solver pave the way for the wide-range operation of dual-mode scramjet burners.

Keywords: *Dual-mode, Free jet, Wide Range, Ramjet*

Nomenclature

$\widetilde{A_k}$ – preexponential factor for reaction step k
C_i – molar concentration of species i
E_{Ak} – the activation energy of reaction step k
g_i – Gibb free energy of i
K_{fk} – forward rate constant for reaction k
K_{bk} – backward rate constant for reaction k
M_i – chemical symbol of i
N_P – exponent of pressure in rate constant of reaction k
N_T – exponent of temperature in rate constant of reaction k
R_0 – universal gas constant
υ'_{ik} – stoichiometric coefficient of i in reactant side of step k
υ''_{ik} – stoichiometric coefficient of i in product side of step k
$\widetilde{W_i}$ – molecular weight of i
ω_{ik} – mass rate per unit volume of production of i form reaction k
F – engine produced net thrust
I_{sp} – engine specific impulse
η – total pressure loss
ε – error compared to finer mesh
T – static temperature

1. Introduction

Many new concepts for high-speed aircraft have been proposed [1, 2], each of which has been proposed to reduce costs, improve safety and improve reliability. Among these candidates shown in Fig. 1 [3], the airbreathing engine seems to be a good choice due to its low payload cost and higher specific impulse [4]. However, it can only be operated within a limited range.

In order to realize the vehicle flight over a wide range of Mach numbers, a combined cycle propulsion system [5, 6] is crucial. This mainly includes turbine-based combined cycle (TBCC), rocket-based combined cycle (RBCC), turbine and rocket based combined cycle (T/RBCC). Although the above concepts have been proposed to broaden the operating range, there are still many problems that need to be solved. These issues involve transonic thrust pinch, low Mach inlet starting, no Mach 4 Turbine Engine, transition thrust pinch, and thermally balanced cruise, as shown in Fig. 2 [7]. In this paper, we focus on Issue 4, where little net thrust will be available for the transition. To solve this problem, our

[1] *Undergraduate, School of Aeronautics and Astronautics, Shanghai Jiao Tong University, E-mail: ludi96@sjtu.edu.cn*
[2] *Associate Professor, School of Aeronautics and Astronautics, Shanghai Jiao Tong University. Corresponding author, E-mail: fangchen@sjtu.edu.cn.*
[3] *Associate Professor, Department of Rocket Engines, Moscow Aviation Institute*
[4] *Professor, School of Aeronautics and Astronautics, Shanghai Jiao Tong University*

approach is to broaden the operating range of the dual-mode ramjet, avoid introducing another engine and try to keep the engine scheme compact and efficient.

Soon after the limitations of supersonic combustion proposed by pioneers [9, 10] to reduce the enormous loss of ramjet were recognized. The concept of a dual-mode ramjet was then proposed by Curran and Stull [8] to operate at both low Mach numbers and high Mach numbers. To date, most recently designed dual-mode scramjets are still based primarily on Curran's concept.

Unlike Curran's concept, Trefney [11] first proposed to operate in a scramjet mode under a ramjet configuration. Fig. 3 shows a schematic of a dual-mode freejet combustor. It consists of a large combustor with a constant geometry and a nozzle throttle with a variable area. In the supersonic combustion mode, an unconstrained free jet passes through the large cavity without impinging on the wall of the combustor. This will bring a range of benefits including enhanced combustion due to shock waves, detonation waves without wall constraints, and elimination of shock/boundary layer interactions. This aerodynamic characteristic of the free jet enables automatic adaptation to the changes in flight conditions without the need to change the cross-section area of the burner. In the subsonic combustion mode, fuel is injected upstream of the terminal shock, followed by diffusion, subsonic combustion, and nozzle acceleration. The combustor works like a conventional ramjet. The transition from subsonic combustion to supersonic combustion is achieved by increasing the throat area of the nozzle to cause separation at the diffuser inlet to transform the terminal shock into a supercritical state. Numerical simulations considering the equilibrium chemistry [11] and the finite rate chemistry [12] of this freejet combustor were carried out to show some of the characteristics of such an idea.

However, there is currently no detailed discussion of the detailed performance of its operation over a wide range of Mach numbers and the different features of different flight Mach numbers. For complex systems, such as dual-mode scramjets, they must be controlled to achieve design tasks [13]. In order to control it well, the key issue is not how much fuel is burned, but the location and organization of combustion [14] to support fuel control and mode transition. Therefore, in this paper, we performed a series of numerical simulations on such freejet engines with fixed geometry on different flight Mach numbers to see their working strategies in the range of flight Mach numbers.

2. Methodology

2.1. CFD++ Overview

This paper uses commercial software CFD++ [15] to simulate the freejet combustion chamber. CFD ++ is a flexible computational fluid dynamics software with a uniform grid, unified physics, and a unified calculation method that can be used to solve steady-state or unsteady, compressible or incompressible NS equations, including multi-component and finite rate chemical modeling. CFD++ also supports a variety of turbulence models that support one to three transport equations. In addition to RANS, CFD++ also supports LES and hybrid LES/RANS methods. Its multi-grid relaxation strategy provides a fast, accurate solution for stable and unsteady flow.

2.2. Geometry and Mesh

The half model used for numerical simulation analysis consists of small straight pipe, divergent pipe, large straight pipe, and curved nozzle. More specifically, a small step is placed at the end of the small straight pipe connecting the small straight pipe and the diverging pipe to facilitate flow separation. The size of the large straight pipe as a combustion chamber is suitable for the combustion of a ramjet engine. Three injectors are used in our model, each injector is located at the center of every third of the inlet area. The main dimensions of the model are given in Fig. 4. The parameters given in Fig. 4 are given in Table 1.

For mesh generation, the coarse mesh consists of 190,000 grid points, the fine mesh consists of 340,000 grid points, and the finer mesh consists of 530,000 grid points. For local mesh refinement, $\Delta s = 2.5 \times 10^{-5}\mathrm{m}$ is applied to the shear layer between air and ethylene, and $\Delta s = 2.5 \times 10^{-6}\mathrm{m}$ is applied to the near wall to ensure that the near wall Y^{+} is close to 1.

2.3. Boundary condition

The incoming flow condition is set to flow for multi-species supersonic flow all condition prescribed. The above boundary conditions are applied to the flow of air and fuel. Table 2 shows the airflow and

fuel conditions for operating conditions at different Mach numbers. The wall of the combustion chamber is considered to be viscous and thermally insulated. The outflow boundary condition is set to the supersonic outflow boundary through the extrapolated value. Also, a symmetry boundary is applied to the centreline.

2.4. Closure Models

Numerical simulations were performed based on the compressible real gas Navier-Stokes RANS equations. The equation of state of the mixture was used to simulate changes in the physical properties of the mixture. The turbulent flow calculation was performed using a Menter Shear Stress Transport (SST) turbulence model. The turbulent Prandtl and Schmidt numbers used in the calculation were 0.9 and 0.5, respectively. A 6-component 3-step Braule ethylene-air chemical reaction mechanism was used in the finite chemical reaction rate to simulate the combustion process.

2.4.1 Reaction Model

For a multicomponent gas mixture reaction with a k-reaction and an i-component, the stoichiometric change from reactant to product can be expressed as Eq. 1:

$$\sum_i \upsilon'_{ik} M_i \leftrightharpoons \sum_i \upsilon''_{ik} M_i \tag{1}$$

Where M_i denotes the concentration of chemical species, υ'_{ik} and υ''_{ik} are stoichiometric coefficients for reactants and products.

The parameters K_{fk} and K_{bk} are the Arrhenius rate constants for forward and backward reactions, and are given by Eq. 2 and Eq. 3:

$$K_{fk} = \widetilde{A_k} T^{N_T} exp(-\frac{E_{Ak}}{R_0 T})(\frac{P}{Patm})^{N_P} \tag{2}$$

$$\frac{K_{fk}}{K_{bk}} = \left(\frac{Patm}{R_0 T}\right)^{\sum_i (\upsilon''_{ik} - \upsilon'_{ik})} \exp\left(-\frac{\Delta \widetilde{G_k}}{R_0 T}\right) \tag{3}$$

Where the change in Gibbs free energy for reaction step k is given by Eq. 4:

$$\Delta \widetilde{G_k} = \sum_{i=1}^{N} \upsilon''_{ik} \widetilde{W_i} g_i - \sum_{i=1}^{N} \upsilon'_{ik} \widetilde{W_i} g_i \tag{4}$$

Finally, the production rate of species i in the reaction step k can be written as Eq. 5:

$$\omega_{ik} = \widetilde{W_i} (\upsilon''_{ik} - \upsilon'_{ik}) [K_{fk} \prod_l C_l^{\upsilon'_{ik}} - K_{bk} \prod_l C_l^{\upsilon''_{ik}}] \tag{5}$$

For example, the 6-species gas model (C2H4, O2, CO, H2, CO2, H2O) is taken into account for chemical reactions. The model considers the following reactions as Eq. 6:

$$\begin{cases} C_2H_4 + O_2 \leftrightharpoons 2CO + 2H_2 \\ 2O + O_2 \leftrightharpoons 2CO_2 \\ 2H_2 + O_2 \leftrightharpoons 2H_2O \end{cases} \tag{6}$$

2.4.2 Turbulence Model

The Reynolds stresses are given by Eq. 7:

$$\rho \overline{u_i u_j} = \frac{2}{3} \delta_{ij} \rho \mathrm{k} - \mu_t S_{ij} \tag{7}$$

in which mean strain and eddy viscosity are given in Eq. 8, Eq. 9:

$$S_{ij} = (\frac{\partial U_i}{\partial x_i} + \frac{\partial U_j}{\partial x_j} - \frac{2}{3} \frac{\partial U_k}{\partial x_k} \delta_{ij}) \tag{8}$$

$$\upsilon_t = \frac{a_1 k}{\max\{a_1 \omega, SF_2\}} \tag{9}$$

Then the whole set of equations including turbulence kinetic energy transport and turbulence inverse time-scale transport are given in Eq. 10:

$$\begin{cases} \frac{\partial \rho \mathrm{k}}{\partial \mathrm{t}} + \frac{\partial}{\partial x_j}(u_j \rho \mathrm{k}) = \widetilde{P_k} - \beta^* \rho \mathrm{k} \omega + \nabla \cdot [(\mu + \sigma_k \mu_t) \nabla \mathrm{k}] \\ \frac{\partial \rho \omega}{\partial \mathrm{t}} + \frac{\partial}{\partial x_j}(u_j \rho \omega) = \frac{\gamma}{\upsilon_t} P_k - \beta \rho \omega^2 + \nabla \cdot [(\mu + \sigma_k \mu_t) \nabla \omega] + 2(1 - F_1) \rho \sigma_{\omega^2} \frac{1}{\omega} \nabla \mathrm{k} \nabla \omega \end{cases} \tag{10}$$

First blending function $\mathrm{k} - \epsilon \rightarrow \mathrm{k} - \omega$ is given in Eq. 11:

$$\begin{cases} F_1 = \tanh\left\{\left\{min\left[max\left(\frac{\sqrt{k}}{\beta^*\omega d}, \frac{500\upsilon}{d^2\omega}\right), \frac{4\rho\sigma_{\omega^2}k}{CD_{k\omega}d^2}\right]\right\}^4\right\} \\ CD_{k\omega} = \max(2\rho\sigma_{\omega^2}\frac{1}{\omega}\nabla \mathrm{k}\nabla\omega, 10^{-10}) \end{cases} \tag{11}$$

Second blending function is given in Eq. 12:

$$F_2 = \tanh\left\{\left[max\left(\frac{2\sqrt{k}}{\beta^*\omega d}, \frac{500\upsilon}{d^2\omega}\right)\right]^2\right\} \tag{12}$$

Limited generation used in k equation is given in Eq. 13:

$$\begin{cases} P_k = [\mu_t\left(\frac{\partial U_i}{\partial x_j} + \frac{\partial U_j}{\partial x_i} + \frac{2}{3}\frac{\partial U_k}{\partial x_k}\delta_{ij}\right) - \frac{2}{3}\delta_{ij}\rho\mathrm{k}]\frac{\partial U_i}{\partial x_j} \\ \widetilde{P_k} = \min(P_k, 10\beta^*\rho\mathrm{k}\omega) \end{cases} \tag{13}$$

The blending of equation is given in Eq. 14:

$$\phi = F_1\phi_1 + F_2\phi_2 \tag{14}$$

In the above, the constants are given in Eq. 15:

$$\begin{cases} \sigma_{k1} = 0.85, \sigma_{\omega 1} = 0.5 \\ \beta_1 = 0.075, \gamma_1 = \frac{\beta_1}{\beta^*} - \sigma_{\omega 1}\kappa^2/\sqrt{\beta^*} \\ \sigma_{k2} = 1.0, \sigma_{\omega 2} = 0.856, \beta_1 = 0.0828 \\ \beta^* = 0.09, \kappa = 0.41, a_1 = 0.31 \\ \gamma_2 = \frac{\beta_2}{\beta^*} - \sigma_{\omega 2}\kappa^2/\sqrt{\beta^*} \end{cases} \tag{15}$$

3. Result and Discussion

3.1. Grid Independence Validation

Before a detailed analysis of the performance of our dual-mode freejet model over a wide range of flight Mach numbers, a grid independent study was first performed to ensure that there is little correlation between the results and the number of grid points. In order to perform such verification, three sets of mesh from coarse to finer are generated, which respectively contain 190000, 340,000 and 530,000 mesh points. The mass averaged physical quantities, including pressure, temperature, Mach number and ethylene mass fraction, and engine performance parameters were used as verification metrics.

From the results given in Fig. 5 and Table 3, we can easily find that all the three grids are fine enough only if for the purpose of evaluating the engine performance, because the performance evaluation of different grids is within 5% error of the finer grid. However, when we focus on the detail features, we can see that the coarse mesh does not describe the details well at some locations, while for fine mesh, the metric values are always within 5% error of the finer mesh. Therefore, taking into account the calculation accuracy and computational efficiency, the fine mesh is used as the final computational grid.

3.2. Operating performance under different Mach number

Boundary conditions given in Table 2 were applied to analyze the performance under different Mach number. The result given in Table 4 shows that the thrust generated under our predefined geometry is negative at Mach 2.5, 3 and 4, while positive thrust is generated at Mach 5, Mach 6 and Mach 8. With the increase of Mach number, the total pressure loss gets greater. From contours showing the specific details of flow field given in Fig. 6, we can find that there are some problems in the flight conditions of low flight Mach number and high flight Mach number.

For the low flight Mach number, from Fig. 6(a), we can see that there is no water component produced in the combustion chamber, which means that weak or even no combustion process takes place. Combined with the temperature contours in Fig. 6(b), we can see that the main cause of weak even non-combustion is the low temperature of the freestream, which means that there is not enough energy to ignite. Therefore, at such a low total temperature, the combustion process hardly occurs by self-ignition, which means that external energy is required for forced ignition in this case.

For the high flight Mach numbers, it can be seen from Fig. 6 that the problem is mainly early combustion, which causes high back pressure and thus induces adverse conditions for fuel injection, which means that a lower equivalence ratio should be applied and fuel addition should be limited.

3.3. Strategy under low flight Mach number

Through the discussion in Section 3.2, we found that under low flight Mach numbers like M2.5 to M4, an ignition source is needed for forced ignition. Therefore, in this section, we will discuss the performance variation by introducing an ignition source at an early stage under such a flight Mach number. To this end, the ignition source is placed in the cavity of the large combustor.

It can be seen from the calculation results given by Fig. 7 that the operating mode of the freejet engine under low flight Mach number is very different from the higher flight Mach number. Compared with the results given in Fig. 6, the combustion mainly occurs in the high-speed core flow at high flight Mach numbers, while at low flight Mach numbers, the combustion mainly occurs in the low-speed recirculation zone of the large combustor, showing two completely different combustion modes. For low speed, combustion is mainly supported by the ignition source and the cavity, while for high-speed, combustion is mainly caused by shock waves.

As shown in Fig. 7, we also found that as the flight Mach number increases, the combustion mode is also undergoing mode transition. At a flight Mach number of 2.5, the combustion process behaves as isobaric combustion and there is a clear boundary between the high-speed core flow region and the low-speed recirculation combustion zone. However, at a flight Mach number of 4.0, the combustion exhibited both low-speed and high-speed characteristics. A portion of the combustion still occurs in the recirculation zone. However, the major portion of the combustion has shifted to the high-speed core flow region and no longer exhibits the clear boundary.

Finally, from the performance results given in Fig. 5, we can find that positive thrust is obtained by the ignition. However, under M2.5 and M3.0, the thrust is still too small, and only when the flight Mach number is turned to M4 can a large thrust be generated to power the flight. On the other hand, with the ignition, the loss of total pressure behaves a drop.

3.4. Strategy under high flight Mach number

Through the discussion in Section 3.2, we found that at high Mach numbers, such as M5 to M6, high fuel-equivalent ratios can cause problems in fuel injection. Therefore, in this section, we will discuss the performance variation under limited equivalence ratio. For this reason, 0.5 is used as a limited equivalence ratio.

From the result of the reduced equivalence ratio given in Fig. 8, we can find that in the case of relatively low equivalence ratio, there is no longer a problem of early combustion causing the high back pressure. And a similar pattern is shown as the Mach 8 case. The flow behaves as if the mainstream first passes through, and then the oblique shock caused by the separation interacts with the mainstream and ignites the mainstream, starting the combustion process. On the other hand, as the flight Mach number increases, the shock position moves significantly backward.

Finally, the performance results given in Table 6 show that the thrust has a slight decrease when the lower equivalence ratio is used. However, still a huge thrust is generated and there is no thrust discontinuity between M5 and M8, which means that there is no working difficulty in the range of M5 to M8.

4. Summary and Conclusion

In the current study, a range of flight Mach numbers were simulated to explore the possibility of a freejet engine solution operating under a wide range. The basic flow characteristic was analyzed and two major combustion structure were found. On the basis of the flow field characteristic, strategies to operate at lower flight Mach number and higher Mach number were proposed.

The major flow field over the range of Mach number consist of a high-speed core flow and a low-speed recirculation zone. At low Mach number, the combustion was majorly organized in the low-speed recirculation zone of the cavity of the huge combustor. While, at high Mach number, the combustion was majorly organized in the high-speed core flow. The two main combustion organization modes are shown, and the operation under M4 is similar to the mixture of two.

On the other hand, at low Mach number, the lower total temperature made it almost unlikely to self-ignition. An early ignition source should be applied in the cavity to promote combustion. While at high Mach number, the equivalence ratio should be under a limit to avoid unadventurous condition for fuel injection.

5. Acknowledgment

The authors gratefully acknowledge the financial support of the National Natural Science Foundation of China (No. 11672183 and 91641129).

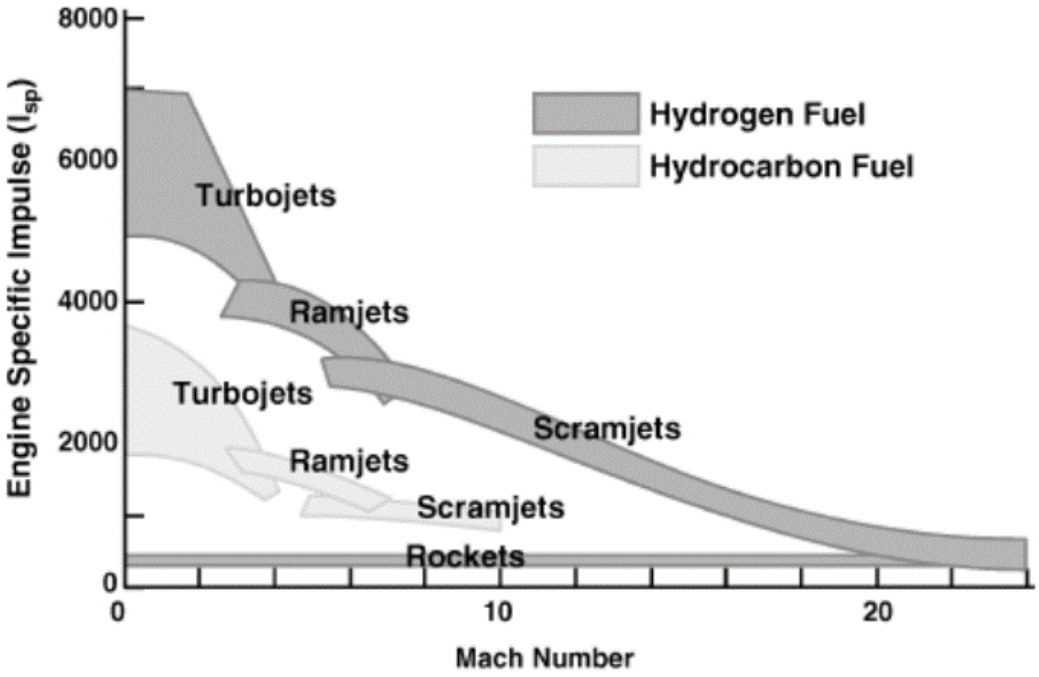

Fig 1. Specific impulses at different Mach numbers [4]

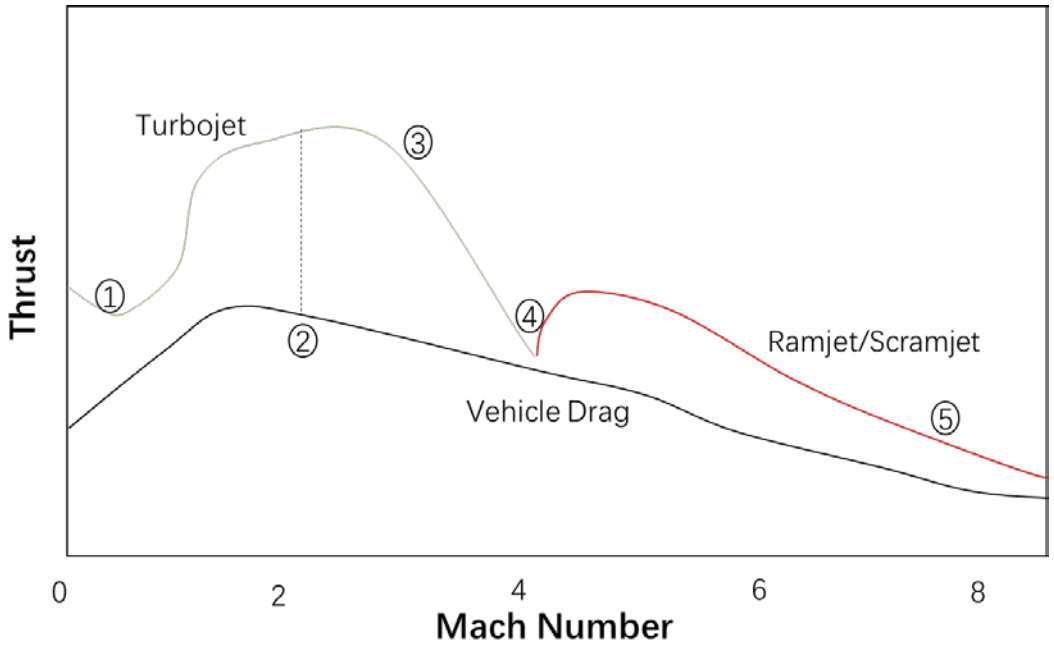

Fig 2. Several difficulties in combining cycle engines [7]

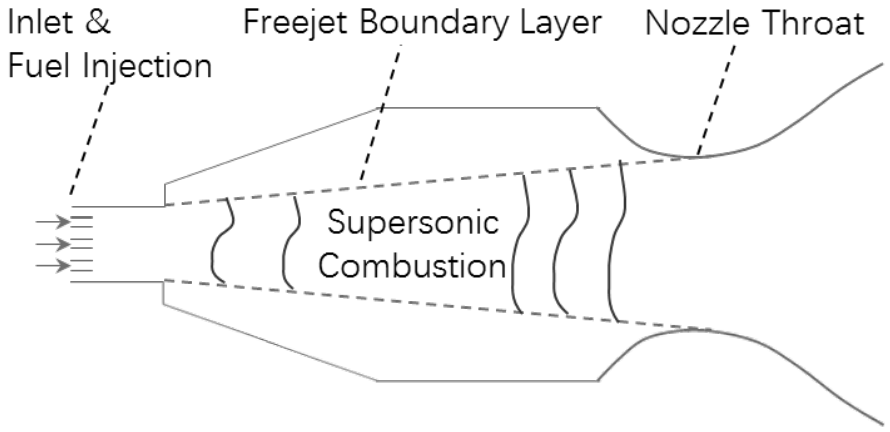

(a) Supersonic free-jet combustion mode

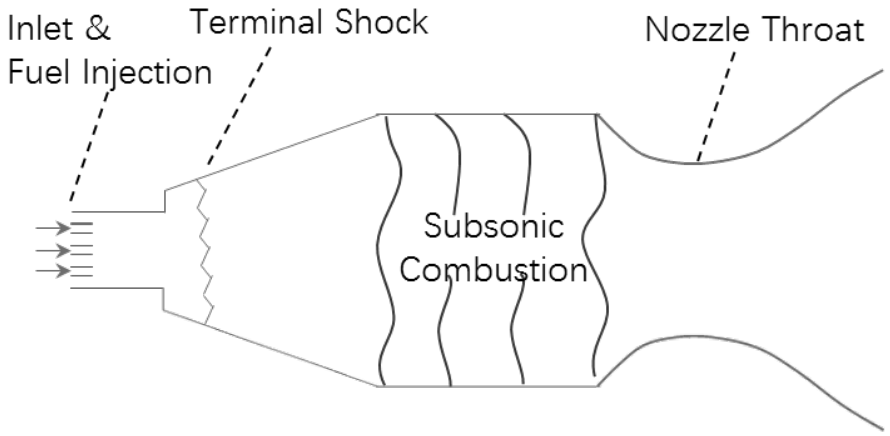

(b) Subsonic ramjet combustion mode

Fig 3. Schematic diagram of the operation of a dual-mode freejet combustion chamber [11]

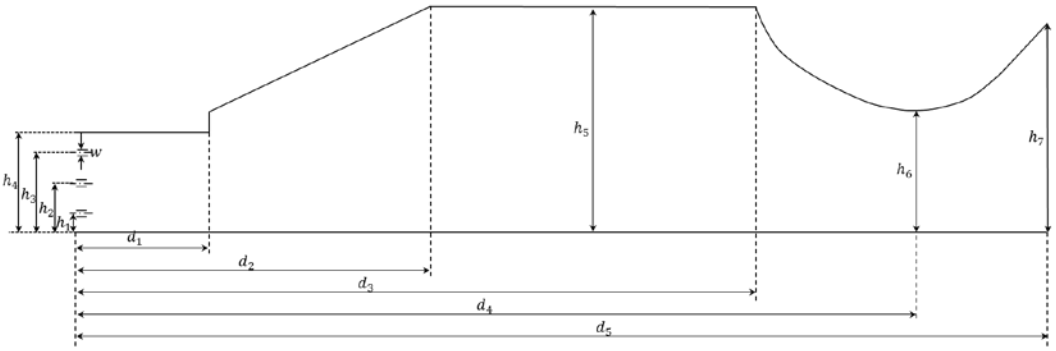

Fig 4. Geometry of the freejet combustor model

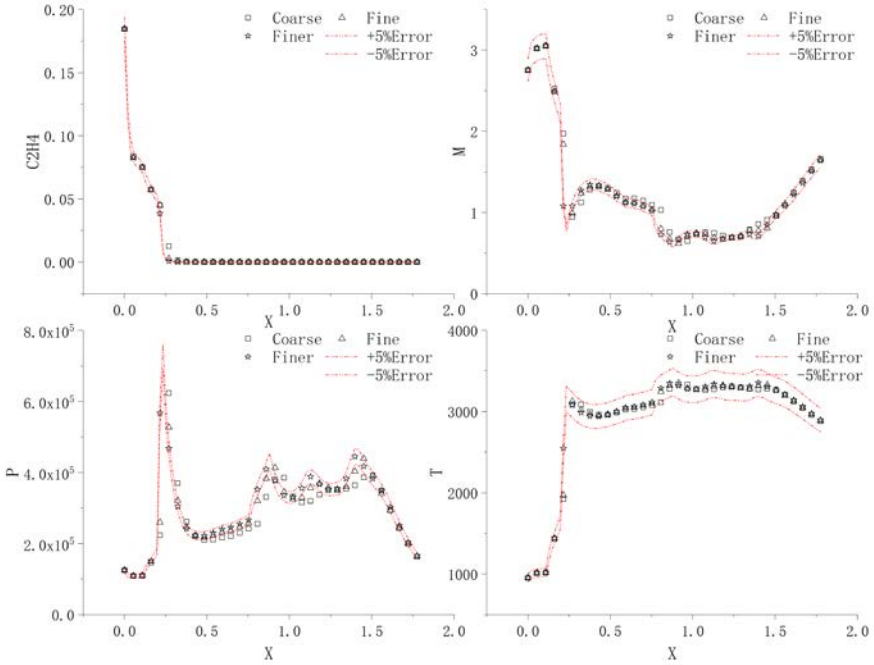

Fig 5. Mass average airflow parameters along the flow direction

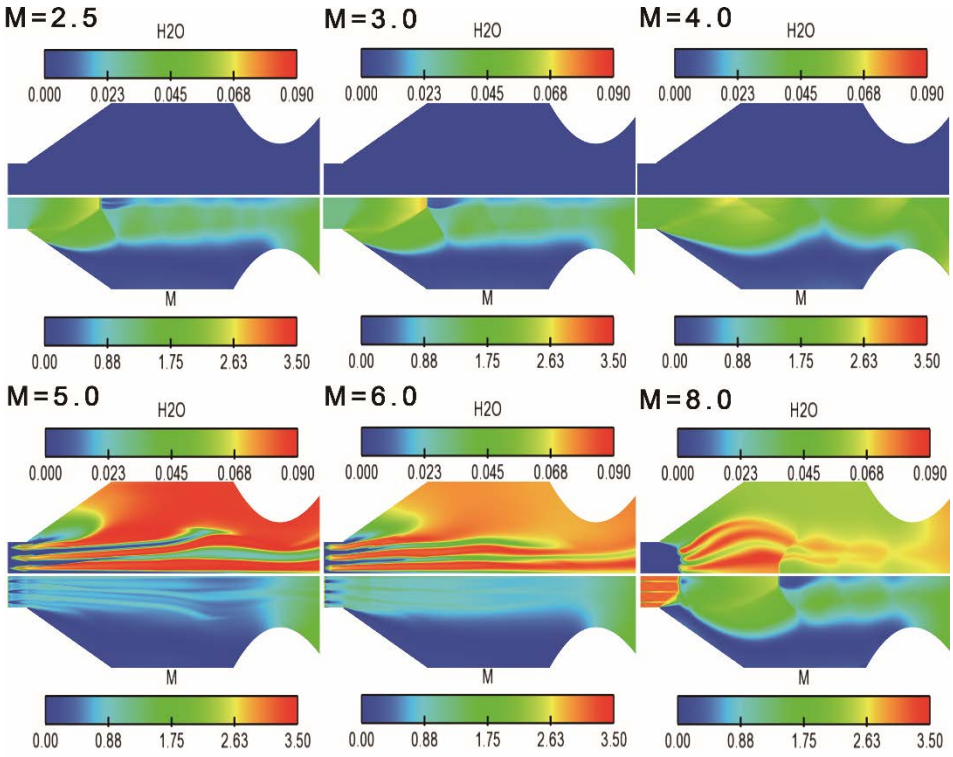

(a) Contours of Mach number and Mass fraction of H2O

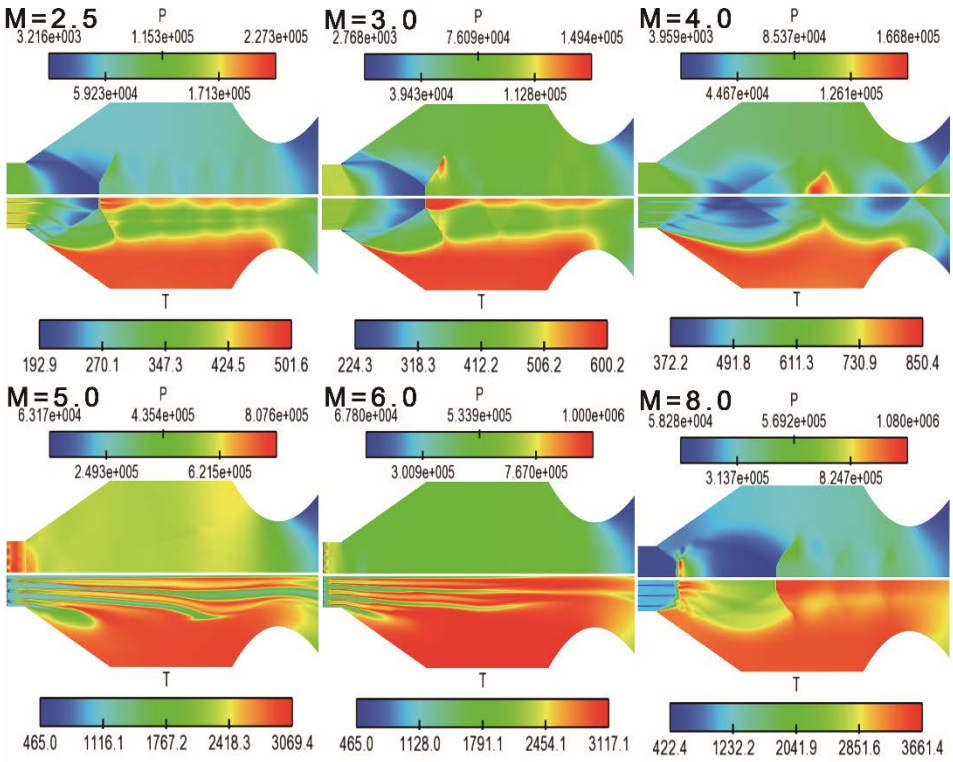

(b) Contours of Pressure and Temperature

Fig 6. Contours of combustion chamber with different flight Mach numbers

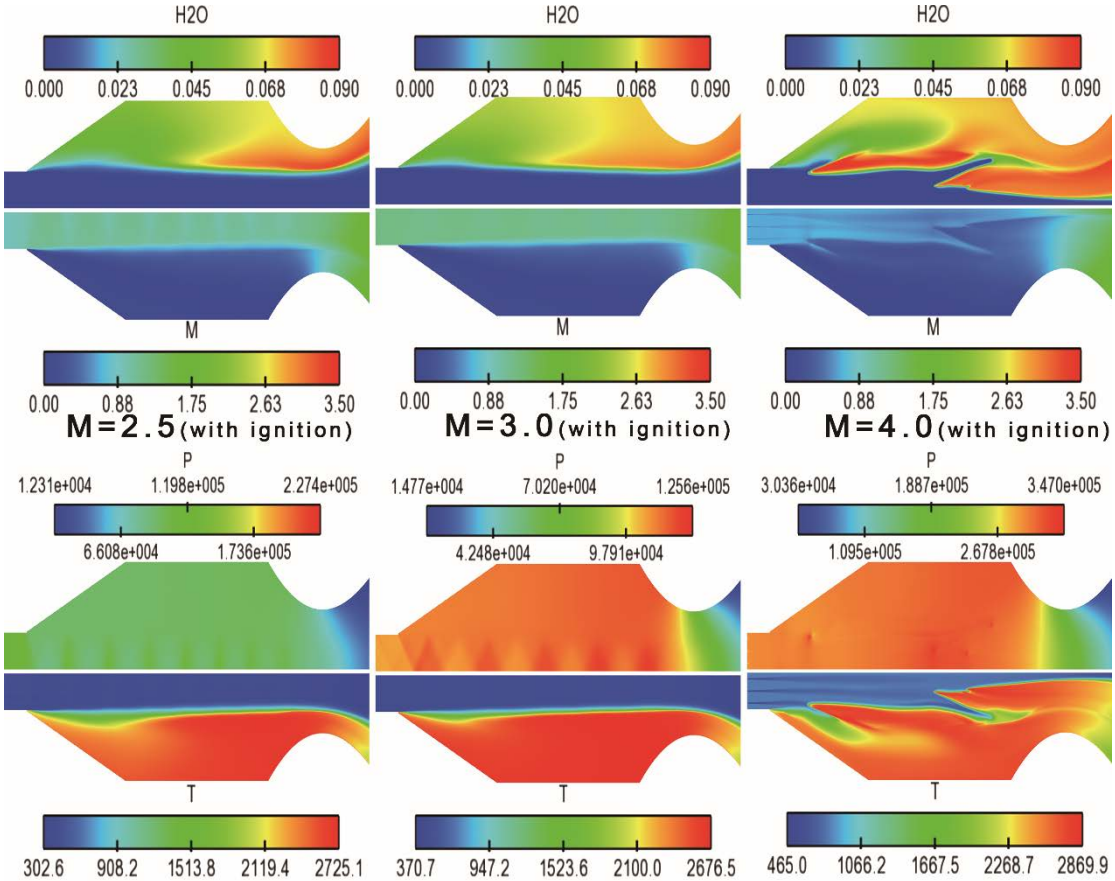

Fig 7. Contours of combustion chamber with ignition source

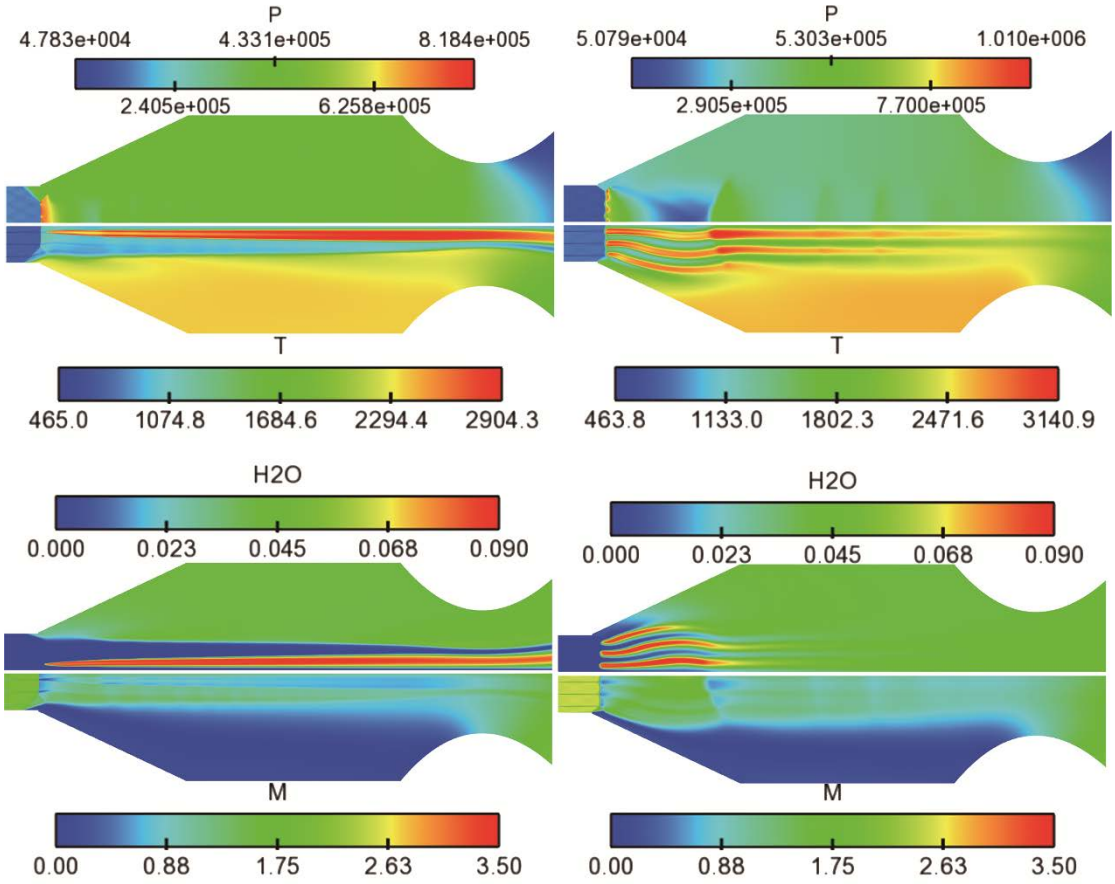

Fig 8. Contours of combustion chamber with lower equivalence ratio

Table 1. Free-jet dual-mode engine model geometry [12]

Symbols	Values(m)
h_1	0.01991
h_2	0.05974
h_3	0.09954
h_4	0.1195
h_5	0.3510
h_6	0.1966
h_7	0.2986
d_1	0.1110
d_2	0.5952
d_3	1.2972
d_4	1.5386
d_5	1.7927

Table 2. Boundary Condition (BC)

Flight Condition	BC(Air)	BC(Fuel)
$M_\infty = 2.5$	$P = 106921.46Pa$	$P = 106921.46Pa$

$H = 13.108km$	$\mathrm{T} = 406.22\mathrm{K}$	$\mathrm{T} = 465\mathrm{K}$
	$\mathrm{M} = 1$	$\mathrm{M} = 1.037$
$\mathrm{M}_\infty = 3$	$\mathrm{P} = 105248.11\mathrm{Pa}$	$\mathrm{P} = 119695.98\mathrm{Pa}$
$H = 15.444km$	$\mathrm{T} = 467.47\mathrm{K}$	$\mathrm{T} = 465\mathrm{K}$
	$\mathrm{M} = 1.22$	$\mathrm{M} = 1.037$
$\mathrm{M}_\infty = 4$	$\mathrm{P} = 97973.01\mathrm{Pa}$	$\mathrm{P} = 136998.71\mathrm{Pa}$
$H = 19.099km$	$\mathrm{T} = 582.87\mathrm{K}$	$\mathrm{T} = 465\mathrm{K}$
	$\mathrm{M} = 1.675$	$\mathrm{M} = 1.037$
$\mathrm{M}_\infty = 5$	$\mathrm{P} = 168037.49\mathrm{Pa}$	$\mathrm{P} = 250066.4\mathrm{Pa}$
$H = 21.952km$	$\mathrm{T} = 730.04\mathrm{K}$	$\mathrm{T} = 465\mathrm{K}$
	$\mathrm{M} = 1.995$	$\mathrm{M} = 1.037$
$\mathrm{M}_\infty = 6$	$\mathrm{P} = 141764.24\mathrm{Pa}$	$\mathrm{P} = 242466.71\mathrm{Pa}$
$H = 24.315km$	$\mathrm{T} = 826.74\mathrm{K}$	$\mathrm{T} = 465\mathrm{K}$
	$\mathrm{M} = 2.44$	$\mathrm{M} = 1.037$
$\mathrm{M}_\infty = 8$	$\mathrm{P} = 108046.62\mathrm{Pa}$	$\mathrm{P} = 205054.36\mathrm{Pa}$
$H = 28.098km$	$\mathrm{T} = 1069.91\mathrm{K}$	$\mathrm{T} = 465\mathrm{K}$
	$\mathrm{M} = 3.08$	$\mathrm{M} = 1.037$

Table 3. Performance under M8 with different mesh size

Mesh	$\mathbf{F(N)}$	$\mathbf{I_{sp}(s)}$	$\boldsymbol{\varepsilon}$
Coarse	69724.12	2541.85	-2.22%
Fine	69906.52	2548.50	-1.96%
Finer	71304.93	2599.48	0

Table 4. Performance under M2.5 to M8

Flight Condition	$\mathbf{F(N)}$	$\mathbf{I_{sp}(s)}$	$\boldsymbol{\eta}$
M2.5	-2575.60	-180.06	0.6027
M3.0	-3332.04	-208.11	0.5803
M4.0	-3380.30	-184.45	0.5435
M5.0	75062.05	2243.98	0.5196
M6.0	83596.20	1735.27	0.3012
M8.0	69906.52	2548.50	0.1227

Table 5. Performance under M2.5 to M4 with ignition

Flight Condition	$\mathbf{F(N)}$	$\mathbf{I_{sp}(s)}$	$\boldsymbol{\eta}$
M2.5	868.86	60.74	0.7239
M3.0	1056.60	65.99	0.7012
M4.0	14639.68	798.83	0.6830

Table 6. Performance under M5 to M6 with lower equivalence ratio

Flight Condition	$F(N)$	$I_{sp}(s)$	η
M5.0	48447.77	1448.35	0.4516
M6.0	56157.43	1731.43	0.2745
M8.0	69906.52	2548.50	0.1227

References

1. J. Liu, H. Yuan, Z. Hua, W. Chen, N. Ge, Experimental and numerical investigation of smooth turbine-based combined-cycle inlet mode transition, Aerosp. Sci. Technol. 60 (2017) 124–130.
2. F. Zuo, G. Huang, C. Xia, Investigation of internal-waverider-inlet flow pattern integrated with variable-geometry for TBCC, Aerosp. Sci. Technol. 59 (2016) 69–77.
3. Fry, Ronald S. "A Century of Ramjet Propulsion Technology Evolution." Journal of Propulsion and Power, Volume 20, No. 1, January-February 2004: 27-58.
4. Huang, Wei, Li Yan, and Jian-guo Tan: Survey on the mode transition technique in combined cycle propulsion systems. Aerospace Science and Technology 39, 685-691 (2014).
5. V. Fernández, G. Paniagua, J. Steelant, Installed performance evaluation of an air turbo-rocket expander engine, Aerosp. Sci. Technol. 35 (2014) 63–79.
6. M.J. Bulman, A. Siebenhaar, Combined Cycle Propulsion: Aerojet Innovations for Practical Hypersonic Vehicles, AIAA Paper 2011-2397, 2011.
7. Bulman M, Siebenhaar A. Combined Cycle Propulsion: Aerojet Innovations for Practical Hypersonic Vehicles[C]// Aiaa International Space Planes and Hypersonic Systems and Technologies Conference. 2011.
8. Curran, Edward T., and Frank D. Stull.: Dual mode supersonic combustion ramjet engine. U.S. Patent No. 3,667,233. 6 Jun. 1972.
9. Ferri A: Possible directions of future research in air-breathing engines. Combustion (1960)
10. Dugger, Gordon L: Comparison of hypersonic ramjet engines with subsonic and supersonic combustion. High Mach Number Air-breathing Engines, Pergamon, Oxford (1961).
11. Trefny, Charles, and Vance Dippold: Supersonic Free-Jet Combustion in a Ramjet Burner. 46th AIAA/ASME/SAE/ASEE Joint Propulsion Conference & Exhibit (2010). https://doi.org/10.2514/6.2010-6643
12. TREFNY, C.J. AND YUNGSTER, S.: Free-Jet Combustor Simulation at Mach 8 Flight Condition. Proceedings of the 35th JANNAF Airbreathing Propulsion Subcommittee Mtg (2016).
13. Harefors, M.: Application of control structure design methods to a jet engine. Journal of Guidance, Control, and Dynamics. 24(3), 510-518 (2001).
14. Micka, D. J., Torrez, S. M., and Driscoll, J. F.: Measurements and Modeling of the Heat Release Distribution in a Dual-mode Scramjet Combustor with Wall Fuel Injection. Proceedings of the 6th U.S. National Combustion Meeting. 12 (2009).
15. METACOMP CFD++ Version 14.1 http://www.metacomptech.com/